



OPEN RF injection scanning tunneling spectroscopy of a superconducting NbSe₂ surface

Md. Arafat Ali¹, Zhipeng Wang^{1,3}, Mohammad Ikram Hossain^{1,3}, Ferdous Ara², Syed Mohammad Fakruddin Shahed² & Tadahiro Komeda^{2,3}✉

NbSe₂ is a transition metal dichalcogenide with a two-dimensional nature, showing superconducting (SC) and charge density properties. Moreover, a 1T phase can be made in the film, which has a different property from the bulk dominant 2H phase, in which Mott insulator behavior is actively discussed. We observed the surface with STM at 400 mK and injected RF signal (1 GHz and 15 Hz) at the tunneling junction. We detected two quasi-particle (QP) states at the end of the SC gap, which split with the increase of the RF power specified by the electric field at the tunneling junction, V_{AC} . A previous STM experiment with 65 GHz RF on a vanadium surface observed multiple replicas of the QP peak. However, our experimental result using 1 GHz RF shows a widening of QP features with two enhanced peaks shifted by $\sim \pm eV_{AC}$ from the original QP positions. The behavior was well reproduced by a simulation using a well-known Tien-Gordon model, whose results indicate that the disappearance of multiple peaks is due to the low frequency of the RF signal. In addition, two enhanced peaks at $\sim \pm eV_{AC}$ are deduced from the Bessel function behavior. The energy shift from the original peak linearly changes with eV_{AC} . We apply this technique to examine the property change at the domain boundary of the 2H and 1T phase of the NbSe₂ surface. We found the superconducting gap decreases when we move the tip from the 2H domain into the 1T domain. Moreover, the injection of RF splits a QP peak into two enhanced peaks, whose energy separation is linear with the electric field at the RF generator for both phases. However, the linear energy separation with V_{AC} shows different coefficients between the 2H and 1T phases. We conclude that the different coefficient is due to the change of actual V_{AC} on the two domains originating from a different dielectric constant and shielding efficiency for the electric field of RF.

Keywords Scanning tunneling microscopy (STM), Photo-assisted-tunneling (PAT), Radio frequency (RF) signal, NbSe₂, Superconductor

Two-dimensional materials attract attention to quantum information technology; especially topological superconductor states are explored for a search of Majorana state that is indispensable for a quantum computer realization¹. NbSe₂ is a transition metal dichalcogenide (TMD) showing superconductivity (SC)². It also shows the charge density wave (CDW) state, and the coexistence of SC and CDW has been an intensive research target. Although the 2H phase dominates in the bulk state, the 1T phase is also observed in a film state. In the 1T phase, NbSe₂ exhibits intriguing properties due to strong electron correlations, including Mott insulating states³. However, recent calculations revealed that the correlation gap was due to charge transfer⁴⁻⁶, not due to a Mott-Hubbard gap, as previously assumed⁷. For the SC property, the bulk NbSe₂ can be described as either a strongly anisotropic s-wave superconductor or a two-gap superconductor⁸⁻¹³, but the investigation into how the electronic state changes in the 1T phase is still ongoing. One of the difficulties in the 1T phase investigation is that it is not the majority phase in the bulk. Thus, developing a surface-sensitive technique to unveil these issues is also essential.

A combination of electromagnetic wave and the scanning probe microscopy has attracted increasing attention. The nanoscale properties of a tunneling region can be identified by employing light waves of different wavelengths. Radiofrequency (RF) signals employed in conventional electron spin resonance spectroscopy can be used with the scanning tunneling microscopy (STM) to detect and manipulate single-electron spins,

¹Department of Chemistry, Graduate School of Science, Tohoku University, 6-3, Aramaki Aza-Aoba, Aoba-ku, Sendai 980-8578, Japan. ²Institute of Multidisciplinary Research for Advanced Materials (IMRAM, Tagen), Tohoku University, 2-1-1, Katahira, Aoba-Ku, Sendai 980-0877, Japan. ³Center for Spintronics Research Network, Tohoku University, 2-1-1 Katahira, Aoba-ku, Sendai 980-8577, Japan. ✉email: tadahiro.komeda.a1@tohoku.ac.jp

as recently demonstrated in experiments^{14–20}. For the working principle of such a single spin detection, an oscillation of a spin by the AC electric field of the RF signal at the tunneling junction (we call V_{AC} hereafter) is attributed. In addition, the scanning tunneling spectroscopy (STS) features of a sharp peak width, like a surface state of coinage metal surfaces, and an inelastic tunneling component of spin excitation, show intriguing changes upon RF injection²¹. The STS can be used to estimate the amplitude of the electric field at the tunneling junction. Hereinafter, we refer to the effect of STS on the RF electric field as the V_{AC} effect.

The phenomenon resulting from the injection of an RF signal into a superconductor–insulator–superconductor (SIS) tunneling junction is known as photon-assisted tunneling (PAT) and has been extensively studied for a long time^{22–24}. The pioneering work of Tien and Gordon revealed that the sharp tunneling feature of an SIS at the edge of a superconductor gap changes into a ladder-like feature owing to the inelastic tunneling process during which energy is gained (lost) by tunneling electrons through the absorption (emission) of multiple photons²⁴. Recently, the PAT measurements have been combined with STM platforms, and phenomena such as multiple Andreev reflections have been observed in various physical systems^{25,26}. However, the application of STM-PAT research for multiple systems has just started.

Herein, we investigate a NbSe₂ surface containing the 2 H phase with 3×3 charge density wave (CDW) reconstruction together with pulse-created 1 T phase of $\sqrt{13} \times \sqrt{13}$ superstructure at the sample temperature of 400 mK and injected RF signal (1 GHz and 15 Hz) at the tunneling junction. We observe two quasi-particle (QP) states at the end of the SC gap, which split with the increased power of the RF. However, unlike a previous STM experiment for the vanadium surface where multiple replicas of the QP peak²⁶, we observe a smooth widening of the QP peak with two enhanced peaks at the energy $\sim eV_{AC}$ shifted from the original position. The behavior was well reproduced by a simulation using the PAT model, revealing the mechanism of the disappearance of the sharp peaks. In addition, we successfully showed the origin of the two enhanced peaks. We apply this technique to investigate property changes at the boundary of 2 H and 1 T phases in the NbSe₂ surface. We found the superconducting gap decreases in energy when we move the tip from the 2 H domain into the 1 T domain. Moreover, the linear energy shift of the RF-induced peaks with RF power shows different coefficients between 2 H and 1 T. We concluded that this change is deduced from a difference in the actual V_{AC} on the two domains, originating from different dielectric constants formed by the insulating nature of the 1 T layer, resulting in a different shielding efficiency for the electric field of RF.

Results and discussions

A NbSe₂ surface was obtained by cleaving the crystal sample in a vacuum. The STM image of the 2 H phase with a superstructure corresponding to a 3×3 reconstruction is shown in Fig. 1, which originates from CDW phase formation^{14–16}. We identified the PAT effect based on changes in STS measurements after RF injection at the tunneling junction. Before presenting the experimental results, we outline our model for the RF effect on the STS, based on PAT theory. PAT was initially proposed to be an inelastic tunneling process involving multiple-photon adsorption and emission. Thus, replicas of the original tunneling peak appear at the positions shifted by a multiple of the photon energy²⁴. The perturbation potential introduced by the RF (photon energy of $\hbar\omega$) is expressed as $eV_{AC}\cos(\omega t)$. The original tunneling conductance $G_{orig}(V_s)$ without RF changes into $G(V_s, V_{AC})$ at a tunneling bias of V_s .

$$G(V_s, V_{AC}) = \sum_{l=-\infty}^{\infty} J_l^2\left(\frac{eV_{AC}}{\hbar\omega}\right) G_{orig}\left(V_s - \frac{l\hbar\omega}{e}\right) \quad (1)$$

where J_l is the Bessel function of the first kind²⁷. In the original report, it was understood that inelastic tunneling peaks involving the absorption and emission of RF photons appear on both sides of the initial peak with an energy shift of $\pm n \hbar \omega$ where n is the number of photons involved in the inelastic process.

While the photon energy level determines the spacing between multiple peaks in PAT, the intensity of the peaks is controlled by V_{AC} contained in the term $J_l^2(eV_{AC}/\hbar\omega)$ of Eq. (1). It exhibits oscillation with V_{AC} , whose frequency and amplitude change with l .

Kot and coworkers demonstrated the PAT process for the vanadium surface at a cryogenic temperature using an STM setup and a superconducting material. They injected RF whose frequency is higher than 65 GHz²⁶. The QP peaks split as the V_{AC} increases. The number of replica peaks and their intensity profile were well reproduced using the Tien-Gordon theory. Individual replicas shifted from the original peaks by $\hbar\omega$ are demonstrated in STS.

Our experimental results for the 2 H phase of the NbSe₂ superconductor surface with the 3×3 superstructure are shown in Fig. 2(a), which displays a series of STS plots with varying V_{AC} of the RF (1 GHz). The starting STS without the RF injection is shown at the bottom of Fig. 2(a), whose quasi-particle (QP) appears at ± 1.0 mV. We can model this spectrum using a Gaussian peak and a step function, which were previously employed²⁸. The results are shown at the bottom of Fig. 2(b); the step function staircases at ± 1.0 mV and the width of the Gaussian function is 1.0 mV.

The width of the STS peak observed on the metal surface is determined by the system temperature, the modulation voltage for the lock-in amp detection, and the intrinsic peak width²⁹. The following equation gives the peak width of W .

$$W = \sqrt{\left(5.4 \frac{k_B T}{e}\right)^2 + (1.7 V_{mod})^2} + W_{int} \quad (2)$$

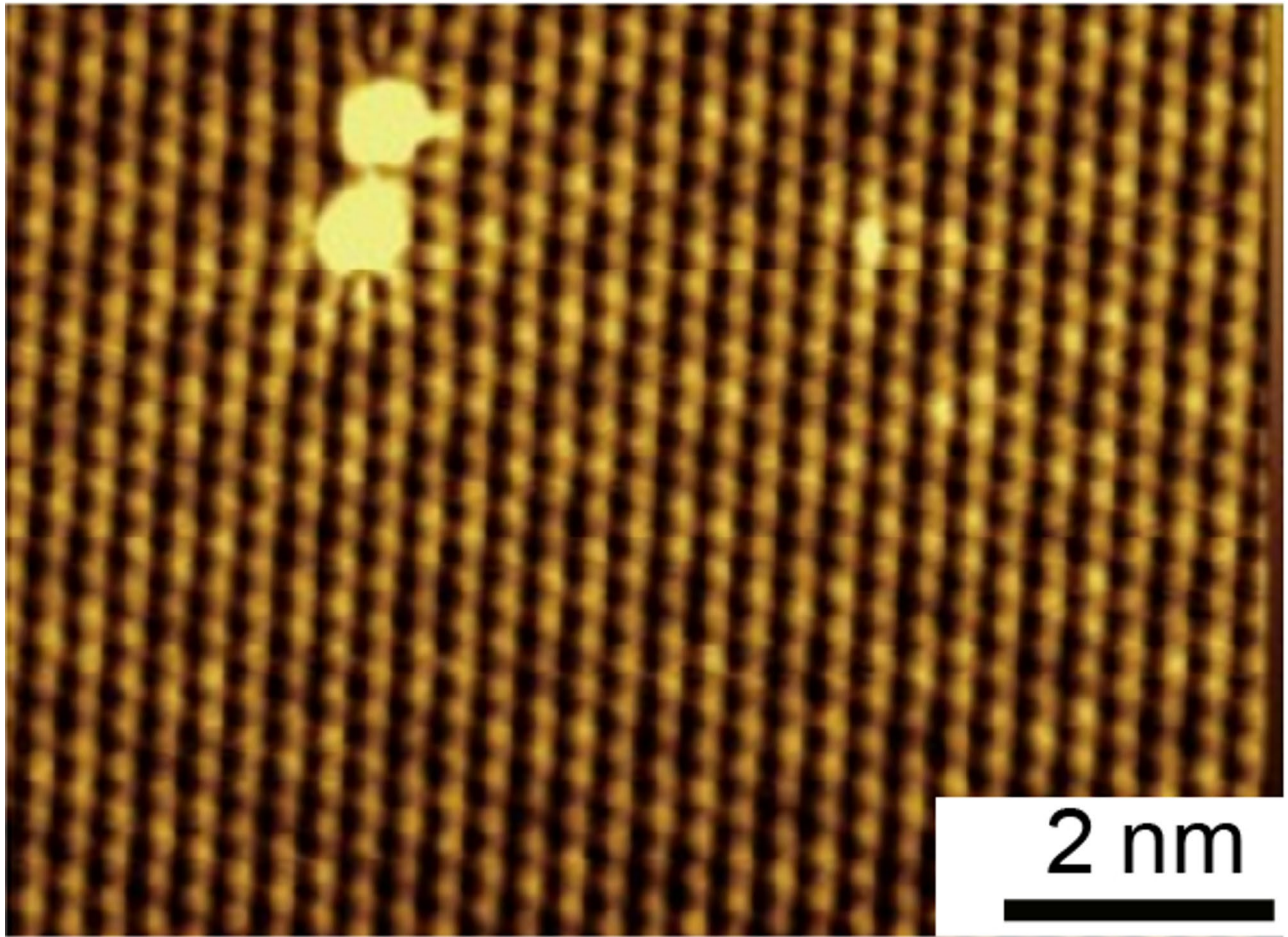


Fig. 1. STM image of the cleaved surface of NbSe₂, showing a 1 H phase with a 3 × 3 reconstructed structure ($V_s = -100$ mV, $I_t = 60$ pA, and scale bar length = 2 nm).

where k_B is the Boltzmann constant, T is the system temperature, V_{mod} is the modulation voltage (rms), and W_{int} is the intrinsic width of the peak. The QP peak broadening can be attributed to the combined effects of these three factors. The thermal broadening originates from the fact that the STM tunneling current is in a closed circuit and thermal equilibrium with the system. We need to lower the system temperature to obtain a narrower peak width, which is determined by the capability of the cryogenic cooling system. A more detailed discussion of the peak width was made by Frenke et al.²⁸.

The RF electric field at the tunneling junction, V_{AC} , was calibrated and correlated with the output at the RF generator ($= V_{\text{AC,gen}}$) using the surface state of Ag surface, which was previously demonstrated^{20,21}, and the details of our analysis are shown in Supplemental Information (SI). This process can obtain the RF signal's power- and frequency-dependent transmission functions and the V_{AC} at the tunneling junction.

With the increase of V_{AC} , each QP peak splits into two, one of which approaches the Fermi level, and the other separates from it. Among the four components that appeared after the RF injection, two components separating from the Fermi level are the dominant peaks for all V_{AC} . The energy shift from the original peak is linear with V_{AC} . The other two components approaching the Fermi level meet at $V_{\text{AC}}=1.0$ mV, and it becomes an enhanced peak at $V_{\text{AC}}=1.4$ mV near the Fermi level. For V_{AC} above 1.4 mV, they move toward the opposite side of the original peak position.

We simulate the evolution of the QPs of the NbSe₂ with V_{AC} using the PAT model and Eq. (1). We assumed that the variable G_{orig} in Eq. (1) is modeled with Gaussian peaks and step function as stated above. Gaussian and step functions were broadened to fit the experimental spectrum. V_{qp} was set to 1.0 mV. The reason of the peak broadening of the STS spectra was explained above. The calculation was done with various V_{AC} , including the ones used in Fig. 2(a). The simulated results, as shown in Fig. 2(b), reproduce the experimental results well, both in terms of energy position and peak shape. The components fanning out from two QP peaks (separating from the Fermi level) are clearly observed as an enhanced feature, while the components initially approaching the Fermi level are enhanced after crossing the Fermi level. The peaks at the top plot marked A and B are originated from positive and negative QP peaks, respectively.

The STS peak positions obtained at different V_{AC} in the simulation results are summarized in Fig. 2(c). We calculated the J^2 value for V_{AC} from 0 mV to 2.4 mV with 0.2 mV increments. Solid squares indicate the positions of the peaks identified in the simulated STS. Due to the broad peak width, some features near the Fermi level are

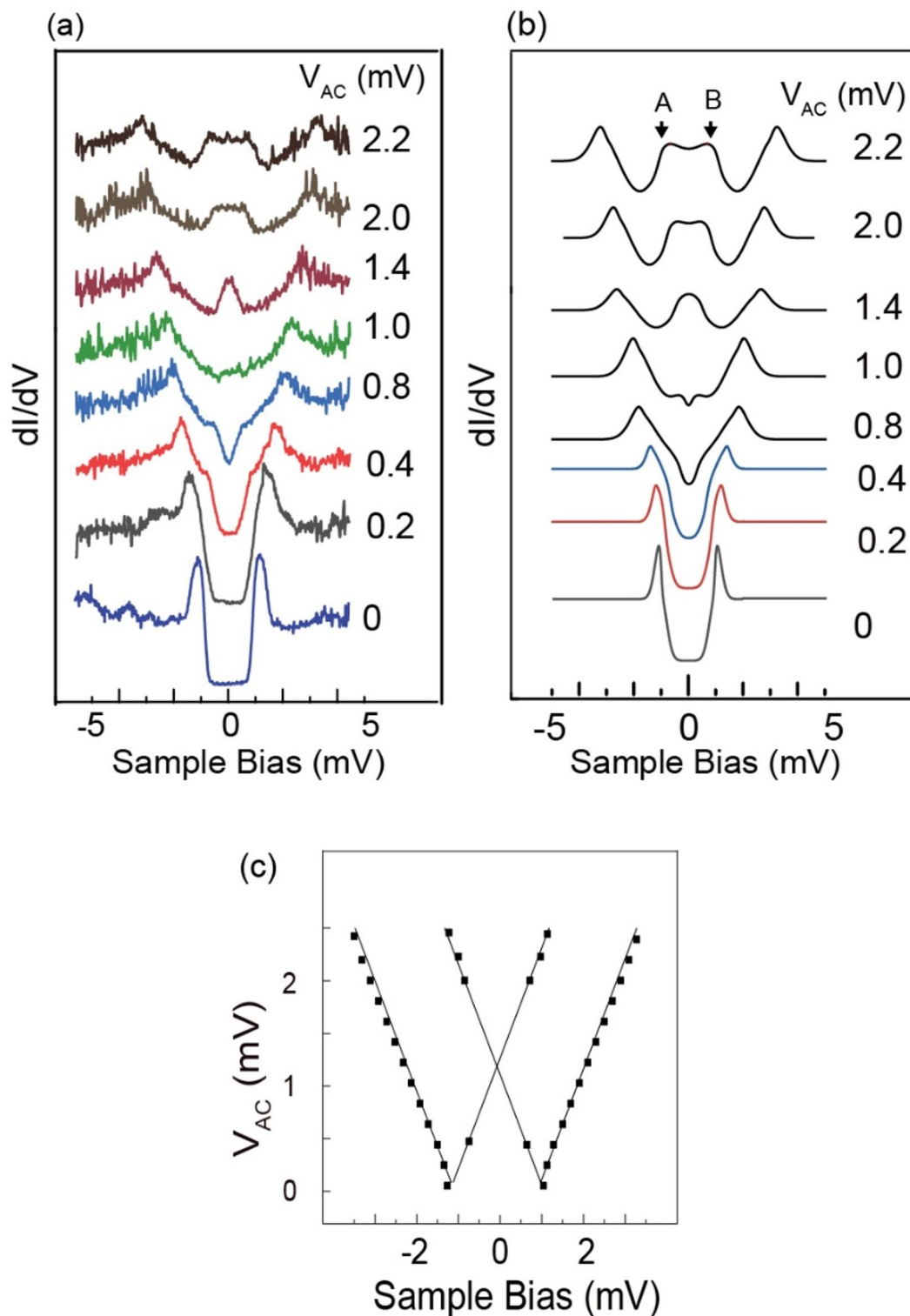


Fig. 2. (a) Experimental results of the dI/dV for the NbSe_2 surface (2 H CDW phase) with the power of RF (1 GHz) at the tunneling junction (indicated as V_{AC} on the right side of each plot). (b) Simulated dI/dV based on Eq. (1), whose eV_{AC} parameters are indicated as V_{AC} for each plot. (c) Variation of the energy position of the dominant peaks of (b). For each V_{AC} , the energy positions of the majority peak are indicated by a small square. The linear line is the fitting result of the least-square method.

not well resolved and omitted. We fit the results with the least-square fitting method, whose result is shown by straight lines in the figure. The slope, $\Delta(\text{position in STS})/\Delta(V_{AC})$ is 1.0 ± 0.01 .

Though experimental results show clear peaks which the PAT model reproduces well, the spectra variation with the RF injection is significantly different from the result of Kot and coworkers introduced above²⁶, in which each QP peak separates into multiple peaks, which are separated by the photon energy. The individual peak corresponds to the number of photons involved. They correspond to $n\hbar\omega$, which are the photons included in the tunneling process.

To understand the mechanism of the discrepancy, we present several simulation examples in Fig. 3 based on the PAT model and Eq. (1); a more elaborate simulation can be found elsewhere^{26,30–32}. The original Tien-Gordon model is sketched in Fig. 3(a) for a case involving only a few photons. When the number of photons increases, the simulated peak shape becomes much more complex, as shown at the bottom of Fig. 3(b). We assume a starting Gaussian peak at the Fermi level and a full width at half maximum (FWHM) of 20 μV . The RF photon energy $\hbar\omega$ is 41.3 μV (10 GHz) and eV_{AC} is 250 μV . RF signal injection forms multiple peaks with a spacing $\hbar\omega = 41.3 \mu\text{V}$. The positions are shifted from the elastic peak by $\pm n\hbar\omega$, and their corresponding energies are determined by the photon energy, independent of V_{AC} .

When the starting Gaussian peak is broader ($D = 100 \mu\text{V}$), most of the sharp peaks are invisible, and only the prominent peaks at $\pm 250 \mu\text{V}$ and the other peaks at $\pm 50 \mu\text{V}$ are visible (see plot II of Fig. 3(b)). We further change the parameters, and the photon energy is changed to a lower energy ($\hbar\omega = 4.13 \mu\text{V}$ corresponding to 1 GHz RF). The peaks near the Fermi level further decreased in height from Plot II, as illustrated in Plot III of Fig. 3(b).

This decrease in the number of sharp peaks from I to II (also from II to III) is mainly due to the shrinking energy spacing between the different n components. When the spacing is small, only the envelope of multiple peaks of the PAT process can be observed. Thus, the final spectrum would be much smoother than Plot I of Fig. 3(b). A similar effect can be expected both for the widening of the original peak and the lowering of the RF photon energy. This smooth feature cannot be attributed to the broadening of the tunneling spectrum because no spectrum broadening mechanism has been incorporated into Eq. (1).

We consider why the two peaks at $\pm V_{AC}$ are enhanced in Fig. 2. The intensity of the sharp peak in Plot I of Fig. 2(b) shows an oscillation with V_{AC} , whose periodicity and maximum intensity changes with l . However, when l becomes large, like one hundred, the change with neighboring l becomes negligible. The smooth spectrum of Plot III of Fig. 3(b) is derived from this effect involving several hundreds of photons. The intensity of each inelastic component can be estimated using the Bessel function. We examine $(J_l(eV_{AC}/\hbar\omega))^2$ vs. l plot where the former term is included in Eq. (1). An example of $(J_l(eV_{AC}/\hbar\omega))^2$ vs. l for $eV_{AC}/\hbar\omega = 100$ is plotted in Fig. 3(c). The $(J_l(V_{AC}/\hbar\omega))^2$ oscillates with l , but the envelope increases slowly and attains its maximum value at $l = 96$, which is close to $V_{AC}/\hbar\omega = 100$. It thereafter rapidly decayed as l continued to increase. The rapid decrease in $(J_l(V_{AC}/\hbar\omega))^2$ for $l > eV_{AC}/\hbar\omega$ is due to the negligible excitation probability for the case where the excitation energy exceeds eV_{AC} , which is the case for the $V_s > \pm eV_{AC}$. The appearance of the maximum value near $|V_s| = \sim V_{AC}$ is why we observe an enhanced peak. Thus, it can fit well with a linear function with a slope of ~ 1 for the QP energy shift vs. eV_{AC} indicated in Fig. 2(c).

To show the photon energy effect in our experiment, we show the case when higher frequency RF ($\hbar\omega = 62.0 \mu\text{V}$, 15 GHz) is used. Experimental results are shown in Fig. 4. The QP feature in STS is shown as Plot I of Fig. 4(a), which changes into Plot II with the RF possessing the electric field at the junction $V_{AC} = 250 \mu\text{V}$. The split peak shows a more complex feature than Fig. 2 obtained with 1 GHz RF. We subtracted the step function and compared the positive and negative QP for more detail. The background and the negative/positive area are specified in the top plot of Fig. 4(a). In the magnified spectra of negative/positive peaks in Fig. 4(b), after the background subtraction. The small features for positive and negative regions in Fig. 4(b) are reproduced with the simulation result at the panel's top. It is intriguing to notice that the features marked by A and B appear similarly in both plots. These features do not mirror the Fermi level but shift equivalent energy from the original peak positions. To show that the minor features are free from noise, we check the sharp peak at position A and a dip at position B, as indicated in Fig. 4(b), which are clearly visible in the negative/positive spectrum. If they are the features of the superconductor, they should appear in the mirror position around the Fermi level, not a parallel shift. Thus, the inelastic feature corresponding to the multiple photon process is used for the case with RF of 15 GHz. This result confirms that the smearing of the peaks to a smooth spectrum is due to the shrinking spacing between multiple components.

Using color mapping, we can observe the variation in the STS results with the RF power (Fig. 5(a)), which is converted from Fig. 2(a) obtained with the 1 GHz RF. The x-axis in Fig. 5(a) represents the sample bias voltage, while the y-axis represents the V_{AC} . The dI/dV value is colored based on the color code at the top of Fig. 5(a). The color of the outward branch shown in Fig. 5(a) changes from red to yellow. The superimposed straight white line, which serves as an eye guide, confirms that the split energy is proportional to the RF electric field.

The inward branch approaching the Fermi level shows an intriguing intensity behavior before and after crossing the Fermi level. This can be visible in the magnified image of Fig. 5(b), in which the crossing occurs near mark A. After crossing, the peak intensity suddenly increases, which is visible as a color change from violet to yellow. Such an increase in intensity cannot be reproduced by Eq. (1). It might be caused by an interference of the two components, but we have to examine it further.

We then examined how the chemical environmental changes affect the RF-induced STS results. For that purpose, we created the 1 T phase area from the 2 H phase of the NbSe₂ surface; the 1 T phase area exhibited a characteristic superstructure of $\sqrt{13} \times \sqrt{13}$ R13.9°, while the 2 H surface exhibited a 3×3 superstructure. The superstructures originated from the CDW^{33–35}, indicating the presence of strong electron interactions^{36,37}.

We formed the 1 T phase by applying a pulse with an amplitude of 3 V and a duration of 10 ms, as reported by Bischoff and coworkers³³. The coexisting newly created 1 T phase and the original 2 H phase are illustrated

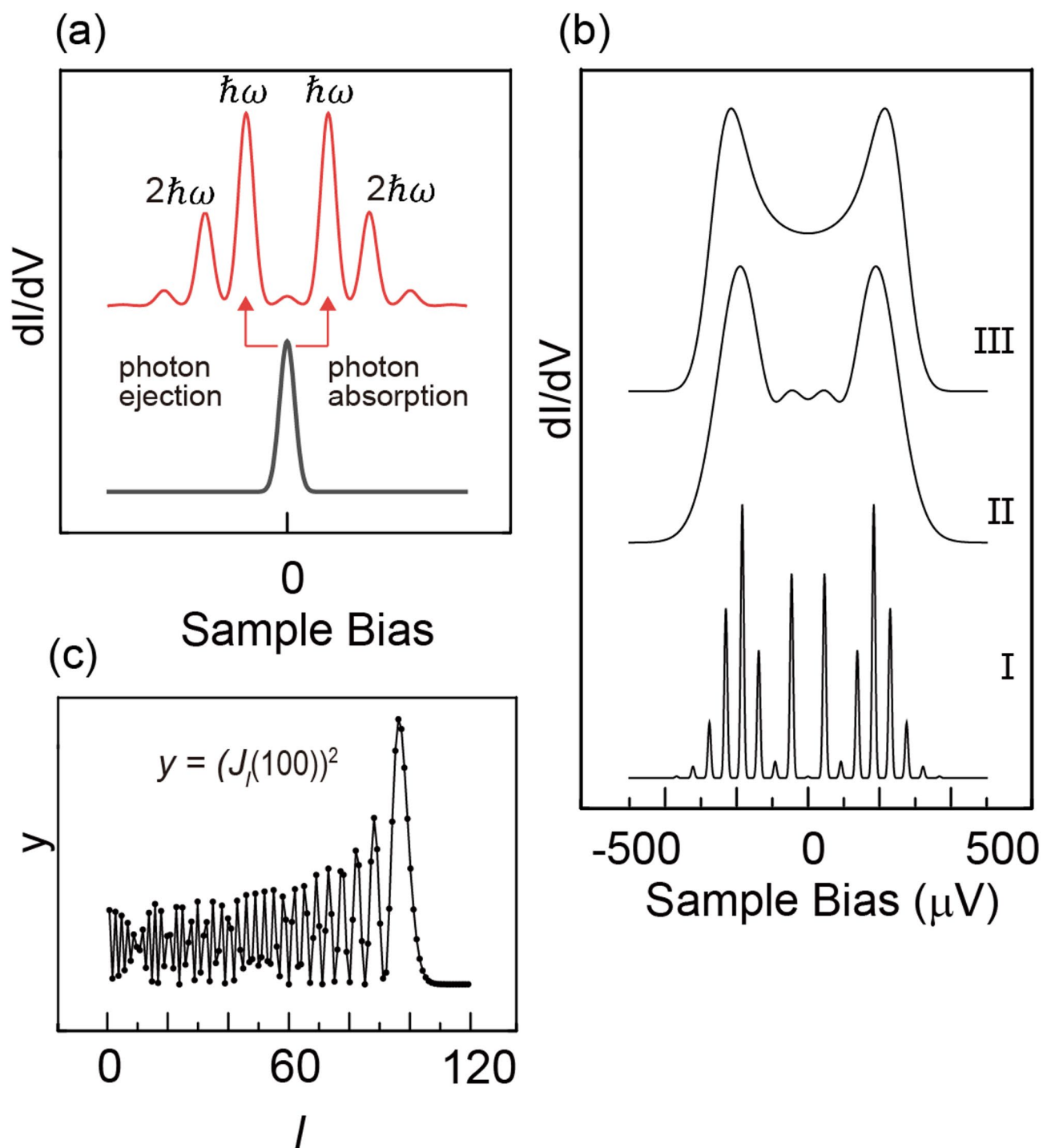


Fig. 3. (a) Schematics of a PAT process involving absorption/emission of multiple photons (photon energy = $\hbar\omega$), whose original peak is plotted by a black line at the bottom as a Gaussian peak. (b) PAT simulation based on Eq. (1). Original Gaussian peak (peak position at the Fermi level) with FWHM width of 20 μV (I) and 100 μV (II, III) are changed with the RF of $\hbar\omega = 41.3 \mu\text{V}$ (I, II) and 4.13 μV (III), whose eV_{AC} is 250 μV (I, II, III). (c) A plot of the square of the Bessel function $(J_l(eV_{AC}/\hbar\omega))^2$ vs. l assuming $eV_{AC}/\hbar\omega = 100$.

in Fig. 6(a), where the $\sqrt{13} \times \sqrt{13}$ R13.9° reconstruction is visible in the upper part of the image (the lower part corresponds to the 3×3 2 H phase, which is less visible than the 1 T phase with an unoptimized tip resolution). The two phases have almost the same height in the topographic image. The 1 T phase refers only to the top layer, and the 2 H phase is below the 1 T phase. As mentioned, the 1 T phase acts as an insulating layer, enabling electrons to tunnel from the 1 T top layer into the 2 H region below.

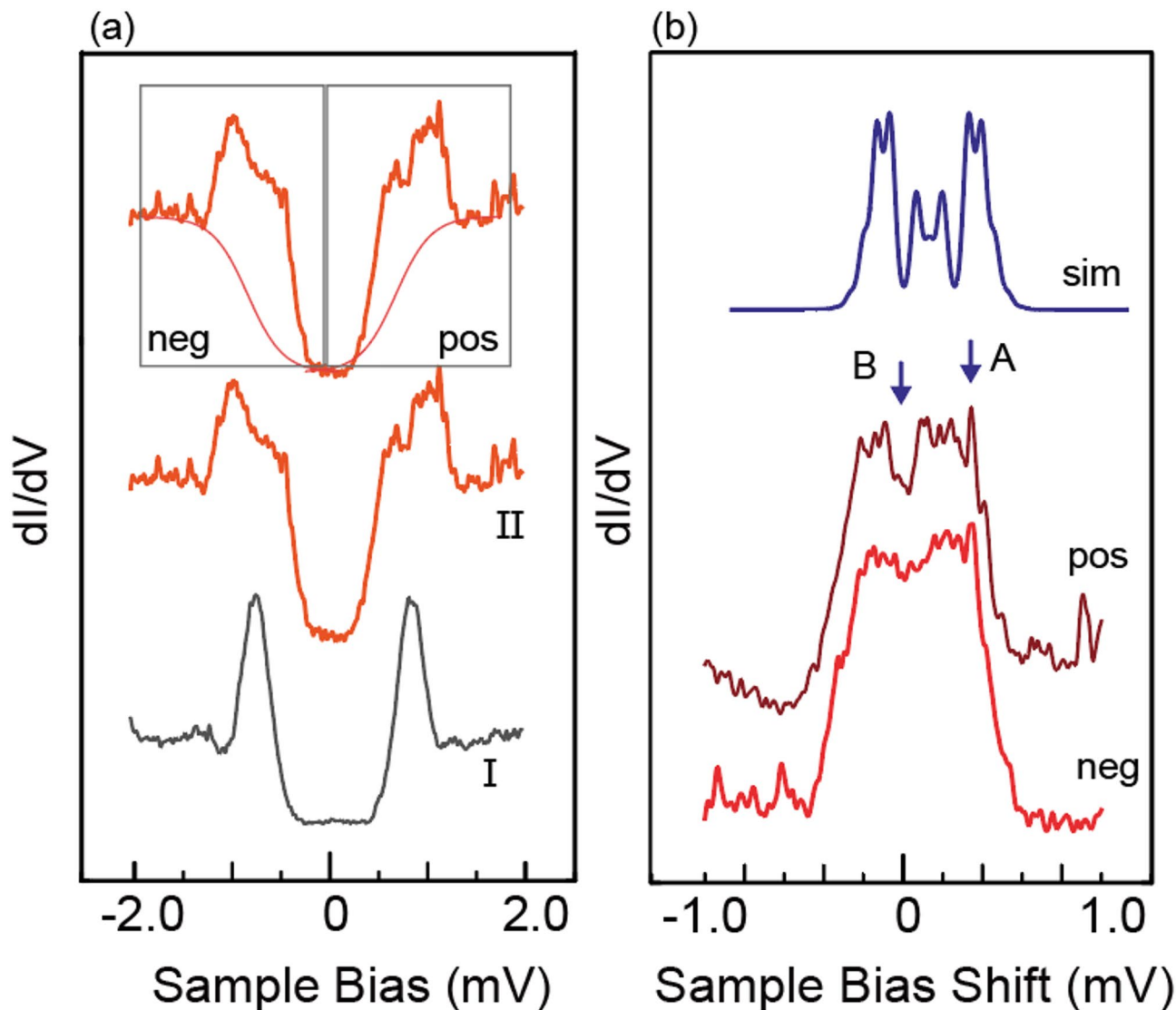


Fig. 4. (a) STS spectrum of the NbSe₂, 2 H phase surface, I, and after injecting RF (15 GHz, V_{AC} is 250 μ V), II. We specify the background and two \tilde{I} components analyzed in (b) on the top panel. (b) The magnified plot of the top panel of (a). The x-axis represents the shift from the original QP position without RF. The top panel shows a simulation result obtained with the PAT method of Eq. (1). (parameters are in the main text).

We compared the RF-induced QP separations observed in the 2 H and 1 T domains. We first measured STS data without an injected RF signal along the white line in Fig. 6(a). The measurement points were numbered (Fig. 6(a)), corresponding to the spectrum with the same number in Fig. 6(b). We determined the peak position by fitting the data with a model stated before: a step function for the SC gap and the Gaussian function²⁸.

The STS series started from the 2 H phase, crossed the 2 H-1T interface, and entered the 1 T phase. The separation of the QP positions was reduced when moving from Spectrum 1 to Spectrum 6. We summarized the position-dependent SC gap (estimated from the energy separations of the two QPs) in Fig. 6(c). The SC gap decreased when the tip position shifted from the 2 H to the 1 T domain, with values of 2.4 meV for the 2 H domain and 1.7 meV for the 1 T domain. The gap size of the 1 T domain was reported to be smaller than that of the 2 H domain, first pointed out by Komori et al. using a bulk sample³⁴. Liu et al. confirmed that an atomically thin 1 T film grown on the graphene surface has a smaller SC gap width than the pristine 2 H phase³⁸. In addition, recent work on TaS₂, a TMD family material, revealed an evolution of the spectra on approaching the step edge at the interface of the 1 T phase and 1 H region, where the QP separation monitors the SC gap. The SC gap shrinks when approaching the 1 T region, which is attributed to the edge mode related to the topological superconducting state³⁹. These observations demonstrate that even a 1 T layer possesses an insulator nature; the spectrum of the 1 T phase is not the spilled state of the underlying 2 H phase but the one characteristic of the 1 T phase.

An alternative mechanism can explain the shrink of the superconductivity gap observed in the 1 T region from the 2 H region. Since it is unclear whether the 1T-phase NbSe₂ preserves the double-gap superconductivity,

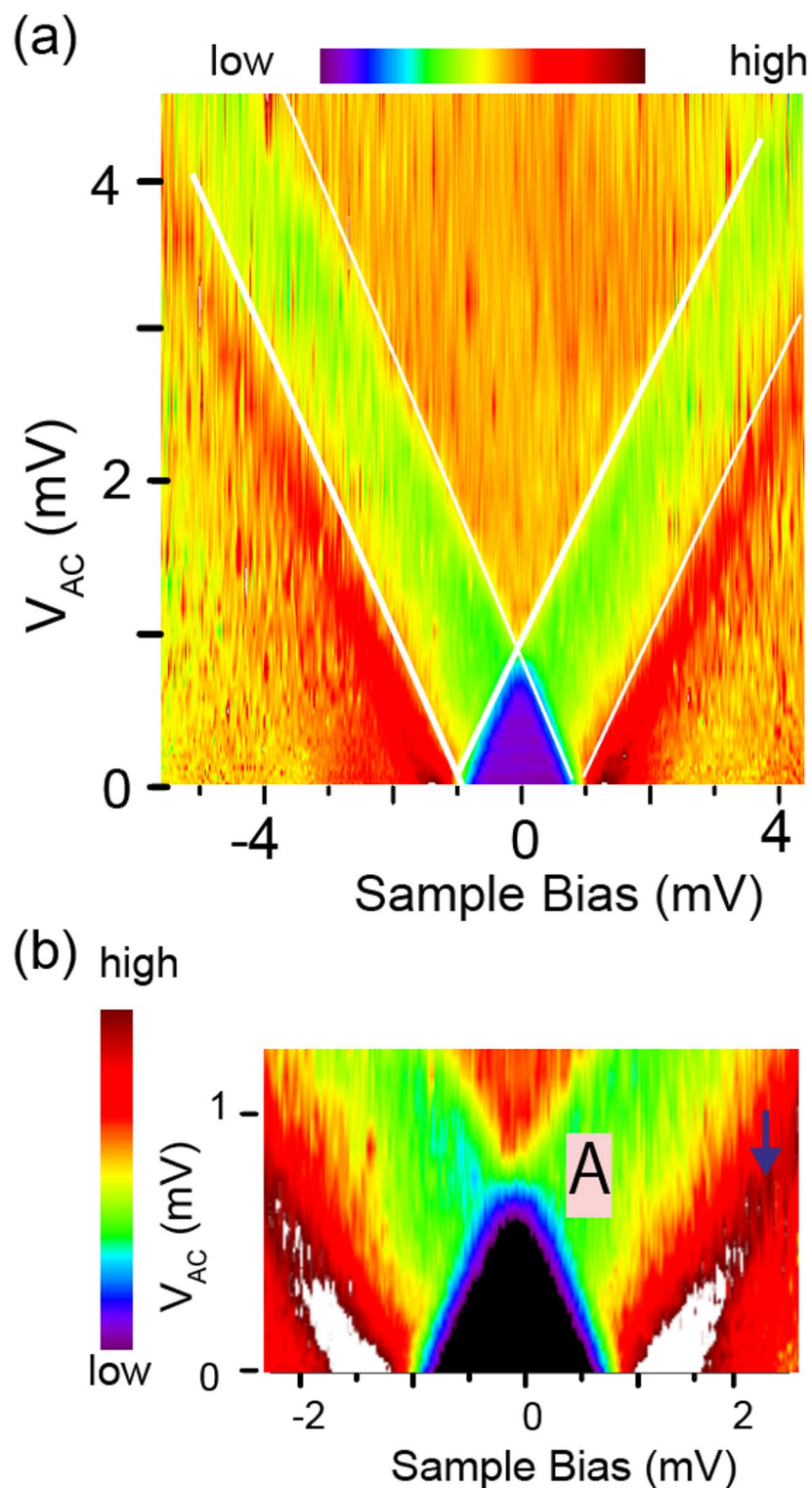


Fig. 5. (a) Color mapping of the STS conductance shown in Fig. 2(a). The x-axis represents the sample bias, while the y-axis represents the RF electric field at the output. The color code adopted is shown at the top. (b) Magnified map of the small RF power area in (a). Mark A shows the position of the crossing of two inward components.

it can change into a single-gap superconductor in the 1T phase. We expect that the width of the QP peak will reduce, and the apparent gap width may shrink depending on which band disappears. When we fit the QP peaks in Fig. 6(b) using the step function and the Gaussian peak, the width is reduced from 0.47 mV for Spectrum 1 to

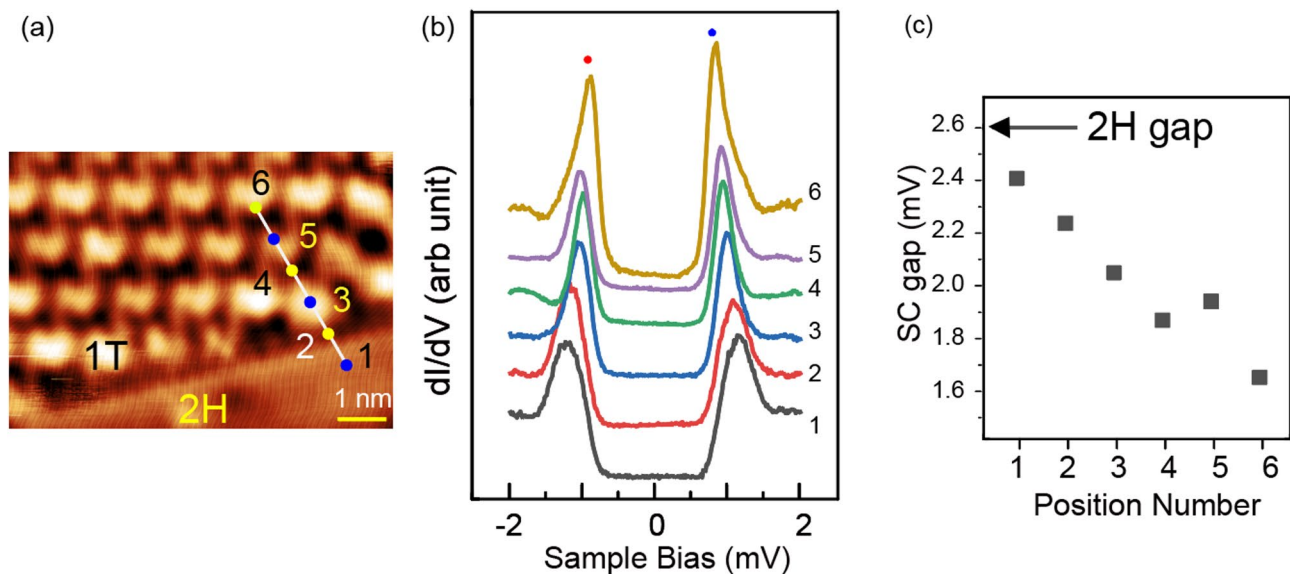


Fig. 6. (a) STM topographic image of the NbSe₂ surface at the domain boundary of the 2H 3×3 and 1T $\sqrt{13} \times \sqrt{13}$ superstructures. ($V_s = -100$ mV, $I_t = 50$ pA). (b) Position-dependent variation of the STS results without RF injection. (c) The gap energy at each position at marks 1–6 specified in (a).

0.31 mV for Spectrum 6. This does not contradict the story we consider above. However, we have to do further investigation to conclude this model.

We then examined the RF-induced QP split. We provide an example in Fig. 7(a), starting on the 2H domain with the RF condition of $V_{AC} = 1.95$ meV and a frequency of 1 GHz. We measured RF-injected STM on the six points in Fig. 6(a). The red and blue dots shown in Fig. 7(b) split into two dots of the same color in Fig. 7(a).

In the above simulation, the positions of the split peaks were symmetric relative to the original peak position. Thus, we examined the center energy of the split peaks and compared the original peak positions without RF injection. We summarized the center energy of the split, represented by red dots in Fig. 7(b), on which the results of Fig. 7(c) without RF have been superimposed. The two series with and without the RF injection agree well, suggesting that the RF splits the original peak with equal energy separation and approaches the Fermi level.

We then analyzed the energy separation of the spectral peaks shown in Fig. 7(a), summarized in Fig. 7(c). The energy separation gradually increased from Position 1 in the 2H domain to Position 6 in the 1T domain after crossing the domain boundary. The density-of-state of the superconducting state increased the energy resolution, which is much better than that obtained for the thermal broadening of the Fermi edge of a typical metal²⁸. Thus, while the thermal broadening of the peak width at 0.4 K is $3.5 \times k_B T = 121$ μ V, an energy shift of a few tens of μ V, as shown in Fig. 7(c), can be detected. We must note that the energy position at a particular surface site is determined by the sum of the site-dependent SC gap change and the RF-induced split energy change. The SC gap shrinks at the inner part of the 1T domain, increasing the split energy. Thus, for example, the blue dots at the sample bias of 3.0 mV seem to stay at a constant energy, but the energy position and the split energies both change with the positions, and we can distinguish them clearly.

The position-dependent RF-induced peak-split energy shown in Fig. 7(c) might indicate this observation technique's applicability to distinguish the surface's chemical variation through different interactions between the surface and the RF signal. However, as we stated before, the STS spectra obtained on the 2H and 1T phase regions are different since the 1T layer is insulating, while the 2H layer is not, causing a double tunneling layer structure. Thus, there is a possibility that the change in the peak separation with RF injection is caused by the difference in the starting dI/dV in the two regions. To examine the effect of the shape of the original spectra on the RF-induced split energy, we compare the simulation results for the 1T and 2H phases. For the original spectrum G_0 of Eq. (1), we use the experimental spectra at marks 1 and 6 of Fig. 6(c) for 2H and 1T phases, respectively. We calculated the STS with Eq. (1) using $eV_{AC} = \pm 2.0$ mV to simulate the RF-induced variation. The pairs of the starting and the simulated spectrum are shown in Fig. 7(d). In the same manner as Fig. 7(a), we mark the separated peaks with the same color circles. Even though the initial peak shape and the QP energy are different for the 2H and 1T phases, the separations for the red circles are almost identical: 3.6710 meV and 3.6665 meV, respectively. The energy difference of 4.5 μ V is orders of magnitude smaller than that shown in Fig. 7(c). We judge the effect of the spectrum shape difference in the RF-induced peak-split energy is negligible.

We show an RF power dependence of Fig. 7(a) feature as a color map in Fig. 8(a). We show the two positions in the 2H and 1T domains, in which the labels of 2H and 1T in the panels specify the measurement positions. In this mapping, we expressed the RF electric field at the power source (instead of at the junction) in the y-axis. The slope of the enhanced peaks is obtained by the least-square method, whose result is shown by white lines for the 2H behavior and black lines for the 1T behavior. We superimposed the result of the 2H phase by white lines onto the 1T panel. It is visible that the slope (V_{AC-gen}/V_{samp}) for the 1T phase is smaller than that for the 2H phase by $\sim 10\%$, which shows a similar value estimated in Fig. 7(c).

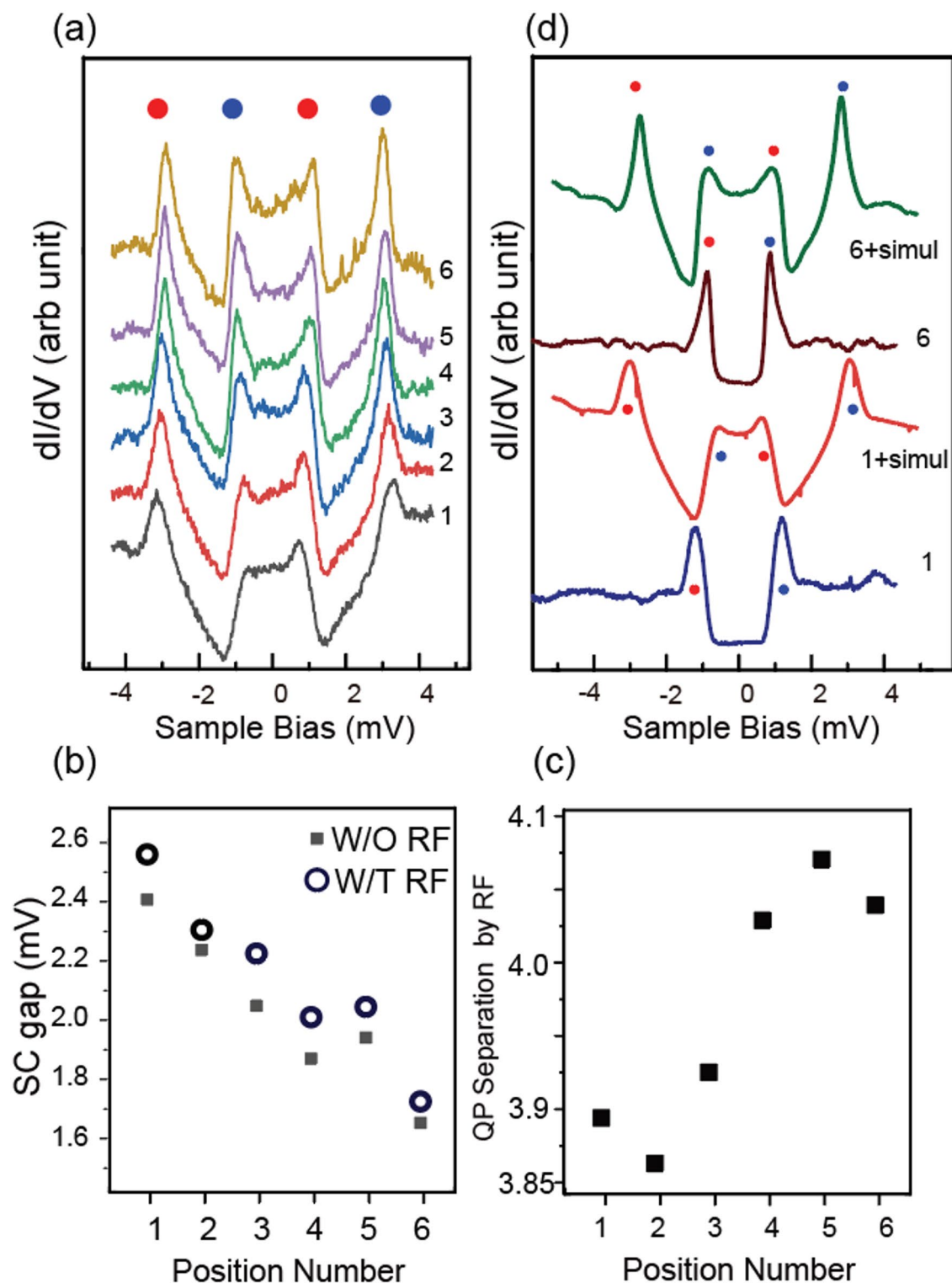


Fig. 7. (a) Site-dependent variation of the QP peaks split by RF, whose V_{AC} is 19.5 mV. Positions from 1 to 6 are marked in Fig. 6(a). The circles with identical colors indicate the pair of divided peaks. (b) Site-dependent SC gap energy estimated by QP peaks without RF (solid circles), and the energy gap of the middle points of the separated peaks (red and blue circles) with RF (open circles). The x-axis indicates the positions are the same as (a). (c) Average of the two split energies (energy between two red dots and energy between two blue dots). Positions 1–6 are identical to (a) and (b). (d) Simulated spectra, starting from the Spectrum 1 and 6 of Fig. 6(b). The color circles guide the identification of the split peak, the same as in (a). The spectra marked 1 + simul, and 6 + simul are simulated results of Eq. (1), in which starting G is regarded as spectrum 1 and 6.

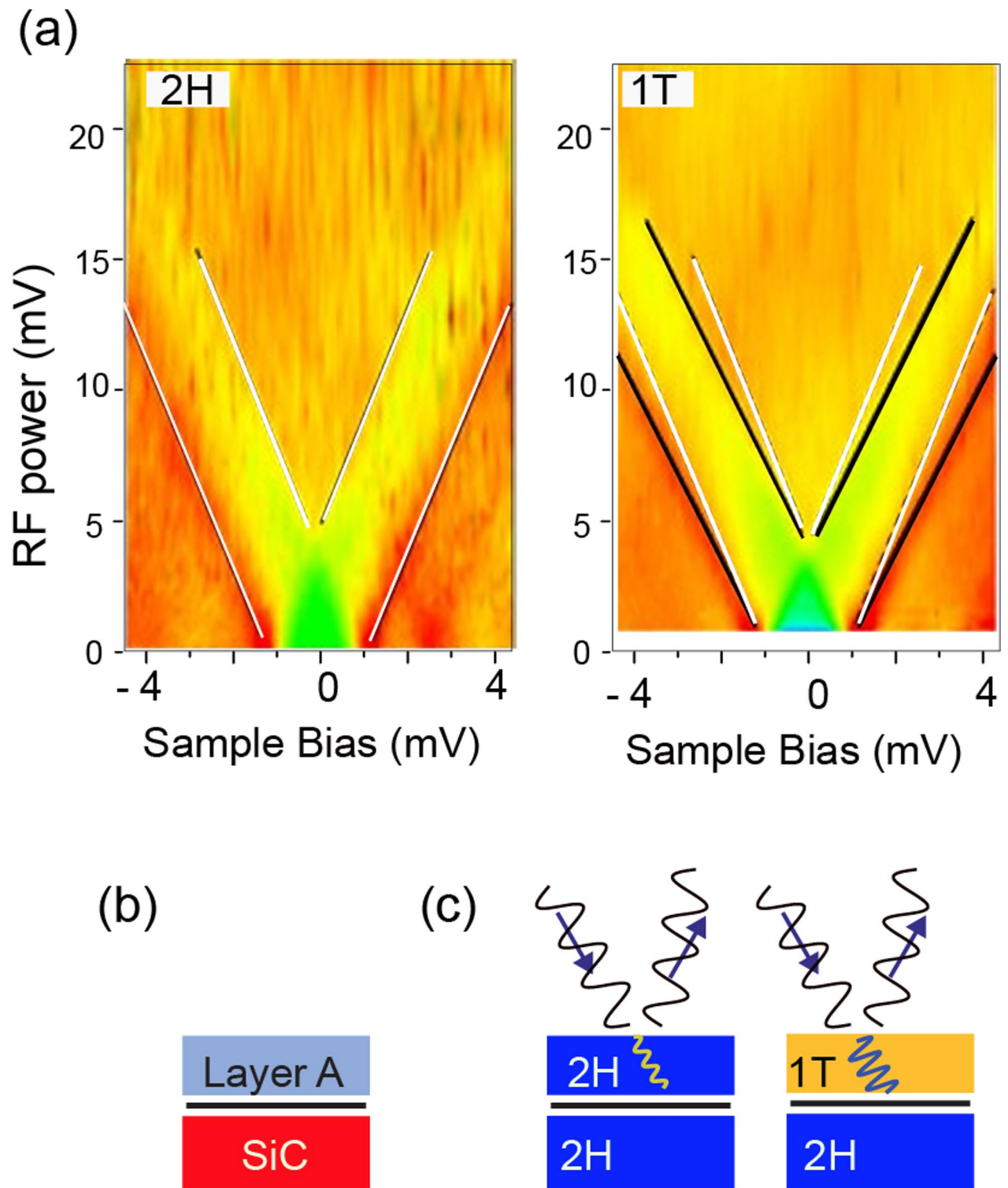


Fig. 8. (a) Color maps of the STS spectra obtained by changing the RF power; the vertical axis represents the electric field at the power source. The tip is positioned at 2 H and 1 T whose spectrum is specified in the figure. Each QP peak at the bottom of the plot is split, and two enhanced peaks appear. The white line shows the linear fitting for the 2 H phase, while the black lines are for the 1 T phase. The results of the 2 H phase is superimposed onto the 1 T panel for a comparison. (b) Schematic of double layer configuration; various overlayer A is on SiC substrate. (c) Side view of NbSe₂ schematics of 2 H and 1 T domains. The sine wave represents the incoming and outgoing RF, illustrating the difference in the penetrating signal in the top layer.

We mention the effect of the tip condition on reproducibility. For the SC material measurement, the tip apex coating with the SC material and the atomic scale geometry affect the STS, especially the SC gap. This is true for our experiment. Thus, the series of spectra shown in the text were obtained by the identical tip.

To explain the different QP splitting energies with the same RF V_{AC} for the 2 H-1T domains, we consider a model in which the actual V_{AC} in the 2 H and 1 T regions differs. For that, we examine previous studies of near-field microwave microscopes (NFMM)^{40–44}, in which the surface conductivity, the dielectric constant, and the capacity of the material surfaces are revealed with the RF injection. A spatial resolution smaller than micrometers, much shorter than the microwave wavelength, can be achieved. To explain the detection mechanism, the distribution of the electric field of the injected RF is discussed^{42,45,46}.

Gu and coworkers simulated the electric field caused by the RF injection for a double-layer configuration depicted in Fig. 8(b)⁴⁷. When the wide-gap semiconductor SiC is placed as the substrate, the RF electric field penetrates the bulk SiC. The electric field is localized beneath the tip but discontinued between the tunneling gap and sample interface owing to the significant impedance mismatch. Consequently, the bulk SiC's electric field is smaller by more than one order of magnitude than the original value. When the atomically thin graphene layer is placed on the SiC (graphene as overlayer A)), the penetrated electric field is further reduced due to the metallic nature of the graphene layer despite its atomically thin thickness. The electric field penetrated SiC is diminished more than several orders of magnitude with the presence of atomically thin graphene. The electric field is reflected toward the tip before reaching the graphene layer.

We apply these simulation results to our case. We can consider a model of the 2 H domain as depicted in Fig. 8(c); the 1 T domain consists of a monolayer of 1 T on top of the 2 H. The STS detects only the top layer's property, and, as we described in the previous paragraph, 1 T and 2 H layers have their characteristic QP features. Thus, the electric field in the 1 T layer determines the split energy. If we compare the insulating 1 T layer and the metallic 2 H layer, a more significant electric field penetrating the top layer is expected when the top layer is 1 T phase. Since the 1 T phase is unstable in the bulk, there is no data on the electric conductivity of 1 T phases. We cannot quantitatively estimate the electric field change, but we expect a significant difference in the electric field penetration. The difference is the origin of the more substantial split of the QP peaks with the same RF power for the 1 T phase than the 2 H phase.

We consider that the PAT on SC works as the microscope, like NFMM, sensing the minute variation of the near-field, RF-induced electric field caused by local chemical environments.

Conclusion

The injected RF signal (1 GHz and 15 Hz) at the tunneling junction makes the QP states at the end of the SC gap split, and the energy position of the split peak changes linearly with the increase of the RF power, V_{AC} . However, the spectrum of the split peak is a smooth curve with two enhanced peaks at the shift position near eV_{AC} instead of discrete replica peaks separated by the photon energy. The behavior was well reproduced by a simulation using the PAT model, revealing that the disappearance of the sharp peaks is the smearing of the multi peaks by broadening the original peak width and/or the shrink of the spacing with lowering the photon energy. In addition, we successfully revealed the origin of the two enhanced peaks near eV_{AC} , which is deduced from the Bessel function. We apply RF injection STS to investigate property changes at the boundary of the 2 H and 1 T phases. We found the superconducting gap decreases when we move the tip from the 2 H domain into the 1 T domain. Interestingly, the linear energy shift of the RF-induced peaks with RF signal's power shows different coefficients between the 2 H and 1 T phases. We concluded that this change is deduced from a difference in the actual V_{AC} on the two domains, originating from different dielectric constants originating from the insulating nature of the 1 T layer, resulting in a different shielding efficiency for the electric field of RF.

Methods

Our experiments employed an ultrahigh vacuum STM (Unisoku, Japan) in which the sample was cooled to 400 mK using ³He. The sample temperature was maintained at 400 mK throughout the experiment. We used PtIr wire as the material for the STM tip. The schematic of the RF injection at the STM tunneling junction is depicted in Fig. 9. We introduce the RF field through SubMiniature version A (SMA) cable, which starts from the output of the RF generator and ends at the anchor point in the UHV using high-frequency compatible connectors, including the feedthrough between the ambient and the vacuum. The anchor point in the UHV is located a few inches from the STM head. From the anchor point, the cable was switched to a thin wire to prevent the mechanical vibration caused by the solid SMA cable. Because the length of this section is short, no significant RF signal loss occurs along it.

The RF signal (1–15 GHz) is introduced to the tunneling junction by superimposing the signal from the RF generator onto the DC tunneling bias voltage using a bias tee connector. The effect of RF injection on the dI/dV spectrum of the QP peaks shown in this manuscript is visible in the continuous wave mode (without RF on/off chopping and lock-in-amplifier). Thus, we continued the RF signal injection during the dI/dV measurement. We superimposed a low-frequency (~ 300 Hz) sinusoidal modulation voltage on the bias voltage to enable STS measurements. The tunneling bias voltage was applied to the STM tip, and the tunneling current was provided from the sample.

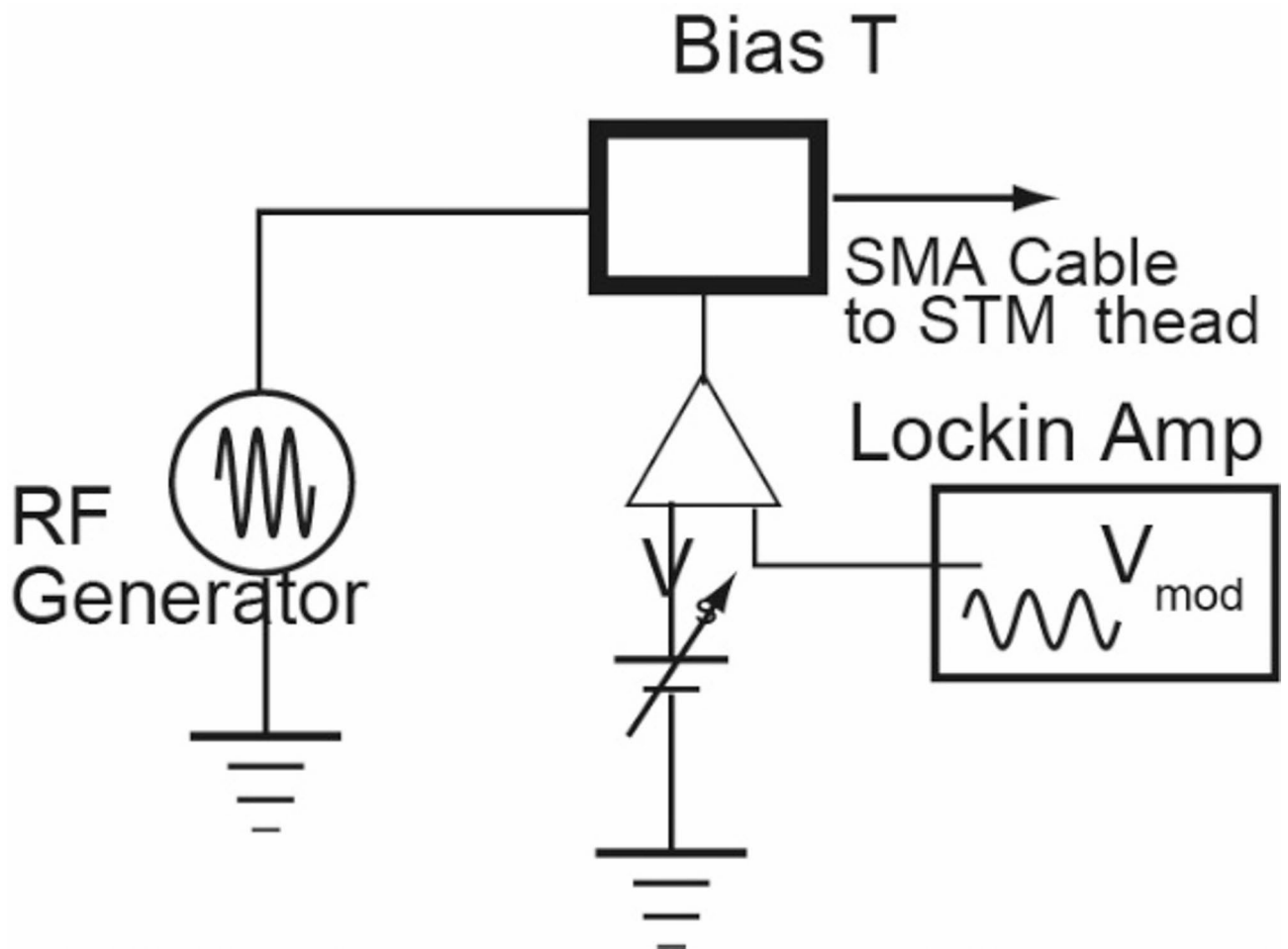


Fig. 9. Schematic showing the injection of the RF signal at the tunneling junction. Tunneling bias is the sum of DC voltage, modulation voltage detected by the lock-in detector, and RF voltage.

Data availability

All data are available in the main text. Any additional data are available from the corresponding author upon request.

Received: 27 November 2024; Accepted: 13 June 2025

Published online: 01 July 2025

References

1. Kitaev, A. Y. Fault-tolerant quantum computation by anyons. *Ann. Phys.* **303**, 2–30 (2003).
2. Gamble, F. R., DiSalvo, F. J., Klemm, R. A. & Geballe, T. H. Superconductivity in layered structure organometallic crystals. *Science* **168**, 568–570 (1970).
3. Chen, Y. et al. Strong correlations and orbital texture in single-layer 1T-TaSe₂. *Nat. Phys.* **16**, 218–224 (2020).
4. Pasquier, D. & Yazyev, O. V. Charge density wave phase, mottness, and ferromagnetism in monolayer 1T-NbSe₂. *Phys. Rev. B.* **98**, 045114 (2018).
5. Calandra, M. Phonon-Assisted magnetic Mott-Insulating state in the charge density wave phase of Single-Layer 1T-NbSe₂. *Phys. Rev. Lett.* **121**, 026401 (2018).
6. Kamil, E. et al. Electronic structure of single layer 1T-NbSe₂: interplay of lattice distortions, non-local exchange, and Mott-Hubbard correlations. *J. Phys. : Condens. Matter.* **30**, 325601 (2018).
7. Nakata, Y. et al. Monolayer 1T-NbSe₂ as a Mott insulator. *NPG Asia Mater.* **8**, e321 (2016).
8. Boaknin, E. et al. Heat conduction in the Vortex state of NbSe₂: evidence for multiband superconductivity. *Phys. Rev. Lett.* **90**, 117003 (2003).
9. Yokoya, T. et al. Fermi surface Sheet-Dependent superconductivity in 2H-NbSe₂. *Science* **294**, 2518–2520 (2001).
10. Zehetmayer, M. & Weber, H. W. Experimental evidence for a two-band superconducting state of NbSe₂ single crystals. *Phys. Rev. B.* **82**, 014524 (2010).
11. Huang, C. L. et al. Experimental evidence for a two-gap structure of superconducting NbSe₂: A specific-heat study in external magnetic fields. *Phys. Rev. B.* **76**, 212504 (2007).
12. Fletcher, J. D. et al. Penetration depth study of superconducting gap structure of NbSe₂. *Phys. Rev. Lett.* **98**, 057003 (2007).
13. Rodrigo, J. G. & Vieira, S. STM study of multiband superconductivity in NbSe₂ using a superconducting tip. *Phys. C: Superconductivity.* **404**, 306–310 (2004).

14. Zhang, X. et al. Electron spin resonance of single iron phthalocyanine molecules and role of their non-localized spins in magnetic interactions. *Nat. Chem.* **14**, 59–65 (2022).
15. Willke, P. et al. Tuning Single-Atom Electron spin resonance in a vector magnetic field. *Nano Lett.* **19**, 8201–8206 (2019).
16. Willke, P. et al. Probing quantum coherence in single-atom electron spin resonance. *Sci. Adv.* **4**, eaaq1543 (2018).
17. Willke, P. et al. Coherent spin control of single molecules on a surface. *ACS Nano.* **15**, 17959–17965 (2021).
18. Yang, K. et al. Engineering the eigenstates of coupled Spin-1/2 atoms on a surface. *Phys. Rev. Lett.* **119**, 227206 (2017).
19. Bae, Y. et al. Enhanced quantum coherence in exchange coupled spins via singlet-triplet transitions. *Sci. Adv.* **4**, eaau4159 (2018).
20. Kawaguchi, R. et al. Spatially resolving Electron spin resonance of π -Radical in Single-molecule magnet. *Nano Lett.* **23**, 213–219 (2023).
21. Paul, W., Baumann, S., Lutz, C. P. & Heinrich, A. J. Generation of constant-amplitude radio-frequency sweeps at a tunnel junction for spin resonance STM. *Rev. Sci. Instrum.* **87**, 074703 (2016).
22. Kouwenhoven, L. P. et al. Photon-assisted tunneling through a quantum Dot. *Phys. Rev. B.* **50**, 2019–2022 (1994).
23. Sweet, J. N. & Rochlin, G. I. Microwave-photon-assisted tunneling in Sn-I-Sn superconducting tunnel junctions. *Phys. Rev. B.* **2**, 656–664 (1970).
24. Tien, P. K. & Gordon, J. P. Multiphoton process observed in the interaction of microwave fields with the tunneling between superconductor films. *Phys. Rev.* **129**, 647–651 (1963).
25. Bruhat, L. E. et al. Scaling laws of the Kondo problem at finite frequency. *Phys. Rev. B.* **98**, 075121 (2018).
26. Kot, P. et al. Microwave-assisted tunneling and interference effects in superconducting junctions under fast driving signals. *Phys. Rev. B.* **101**, 134507 (2020).
27. Falci, G., Bujanja, V. & Schön, G. Quasiparticle and Cooper pair Tunneling in small capacitance Josephson junctions - Effects of the electromagnetic environment. *Z. Für Physik B Condens. Matter.* **85**, 451–458 (1991).
28. Franke, K. J., Schulze, G. & Pascual, J. I. Competition of superconducting phenomena and Kondo screening at the nanoscale. *Science* **332**, 940–944 (2011).
29. Hallböök, A. S., Oncel, N., Huskens, J., Zandvliet, H. J. W. & Poelsema, B. Inelastic electron tunneling spectroscopy on decanethiol at elevated temperatures. *Nano Lett.* **4**, 2393–2395 (2004).
30. Roychowdhury, A., Dreyer, M., Anderson, J. R., Lobb, C. J. & Wellstood, F. C. Microwave photon-assisted incoherent cooper-pair tunneling in a Josephson STM. *Phys. Rev. Appl.* **4**, 034011 (2015).
31. Peters, O. et al. Resonant Andreev reflections probed by photon-assisted tunnelling at the atomic scale. *Nat. Phys.* **16**, 1222–1226 (2020).
32. Gruber, M., Weismann, A. & Berndt, R. The Kondo resonance line shape in scanning tunnelling spectroscopy: instrumental aspects. *J. Phys. Condens. Matter.* **30**, 424001 (2018).
33. Bischoff, F. et al. Nanoscale phase engineering of Niobium diselenide. *Chem. Mater.* **29**, 9907–9914 (2017).
34. Komori, F., Iwaki, T., Hattori, K., Shiino, O. & Hasegawa, T. New superstructure on the surface of 2H-NbSe₂ and tunneling spectra at 4.2 K. *J. Phys. Soc. Jpn.* **66**, 298–301 (1997).
35. Wang, H., Lee, J., Dreyer, M. & Barker, B. I. A scanning tunneling microscopy study of a new superstructure around defects created by tip-sample interaction on 2H-NbSe₂. *J. Phys. Condens. Matter.* **21**, 265005 (2009).
36. Chatterjee, U. et al. Emergence of coherence in the charge-density wave state of 2H-NbSe₂. *Nat. Comm.* **6**, 6313 (2015).
37. Arguello, C. J. et al. Visualizing the charge density wave transition in 2H-NbSe₂ in real space. *Phys. Rev. B.* **89**, 235115 (2014).
38. Liu, M. et al. Monolayer 1T-NbSe₂ as a 2D-correlated magnetic insulator. *Sci. Adv.* **7**, eabi6339 (2021).
39. Nayak, A. K. et al. Evidence of topological boundary modes with topological nodal-point superconductivity. *Nat. Phys.* **17**, 1413–1419 (2021).
40. Tabib-Azar, M., Su, D. P., Pohar, A., LeClair, S. R. & Ponchak, G. 0.4 μm Spatial resolution with 1 ghz ($\lambda = 30$ cm) evanescent microwave probe. *Rev. Sci. Instrum.* **70**, 1725–1729 (1999).
41. Imtiaz, A. & Anlage, S. M. A novel STM-assisted microwave microscope with capacitance and loss imaging capability. *Ultramicroscopy* **94**, 209–216 (2003).
42. Imtiaz, A., Baldwin, T., Nembach, H. T., Wallis, T. M. & Kabos, P. Near-field microwave microscope measurements to characterize bulk material properties. *Appl. Phys. Lett.* **90**, 243105 (2007).
43. Hovsepian, A. et al. Direct imaging of photoconductivity of solar cells by using a near-field scanning microwave microprobe. *J. Appl. Phys.* **106**, 11490 (2009).
44. Kim, J. et al. Investigation of photoconductivity of silicon solar cells by a near-field scanning microwave microscope. *Ultramicroscopy* **109**, 958–962 (2009).
45. Tselev, A. et al. Near-field microwave scanning probe imaging of conductivity inhomogeneities in CVD graphene. *Nanotechnology* **23**, 385706 (2012).
46. Anlage, S. M., Talanov, V. V. & Schwartz, A. R. in *Scanning Probe Microscopy* Vol. 2 215–253 Springer New York, (2007).
47. Gu, S., Zhou, X., Lin, T., Happy, H. & Lasri, T. Broadband non-contact characterization of epitaxial graphene by near-field microwave microscopy. *Nanotechnology* **28**, 335702 (2017).

Acknowledgements

This study was supported in part by Grant-in-Aid for Scientific Research (S) (No.19H05621), and (B) (No. 24K01339). Grant-in-Aid for Transformative Research Areas No. 25H02109 (Tadahiro Komeda) and Grant-in-Aid for Scientific Research (C) (No.21K04873) (Syed Mohammad Fakruddin Shahed).

Author contributions

M.A., Z.W., M.H., J.A., and S.S. all contributed equally to the experimental procedure. M.A. wrote and edited the manuscript. T.K. made the experimental plan and supervised both the experiments and the manuscript writing.

Declarations

Competing interests

The authors declare no competing interests.

Additional information

Supplementary Information The online version contains supplementary material available at <https://doi.org/10.1038/s41598-025-07203-2>.

Correspondence and requests for materials should be addressed to T.K.

Reprints and permissions information is available at www.nature.com/reprints.

Publisher's note Springer Nature remains neutral with regard to jurisdictional claims in published maps and institutional affiliations.

Open Access This article is licensed under a Creative Commons Attribution 4.0 International License, which permits use, sharing, adaptation, distribution and reproduction in any medium or format, as long as you give appropriate credit to the original author(s) and the source, provide a link to the Creative Commons licence, and indicate if changes were made. The images or other third party material in this article are included in the article's Creative Commons licence, unless indicated otherwise in a credit line to the material. If material is not included in the article's Creative Commons licence and your intended use is not permitted by statutory regulation or exceeds the permitted use, you will need to obtain permission directly from the copyright holder. To view a copy of this licence, visit <http://creativecommons.org/licenses/by/4.0/>.

© The Author(s) 2025